Title: Activity of human-specific Interlaminar Astrocytes in a Chimeric Mouse Model of Fragile X Syndrome

Running Title: Calcium signaling of human interlaminar astrocytes

Authors: Alexandria Anding[1,*], Baiyan Ren[2,*], Ragunathan Padmashri[3,*], Maria Burkovetskaya[3] and Anna Dunaevsky[3,#]

#Correspondence:
Anna Dunaevsky
adunaevsky@unmc.edu
*These authors contributed equally

[1]Department of Genetics Cell Biology and Anatomy, University of Nebraska Medical Center.
[2] Department of Biochemistry and Molecular Biology, University of Nebraska Medical Center.
[3]Department of Neurological Sciences, University of Nebraska Medical Center, Omaha, NE 68198, USA

Acknowledgements
This work was supported by Nebraska Stem Cell Grant, Edna Ittner Pediatric Research Support Fund and R21NS122157 to A.D.

Abstract

Astrocytes, a type of glial cells, have multiple roles in regulating neuronal development and homeostasis. In addition to the typical mammalian astrocytes, in the primate cortex interlaminar astrocytes are located in the superficial layer and project long processes traversing multiple layers of the cerebral cortex. Previously, we described a human stem cell based chimeric mouse model where interlaminar astrocytes develop. Here, we utilized this model to study the calcium signaling properties of interlaminar astrocytes. To determine how interlaminar astrocytes could contribute to neurodevelopmental disorders, we generated a chimeric mouse model for Fragile X syndrome. We report that FXS interlaminar astrocytes exhibit hyperexcitable calcium signaling and cause an increase in dendritic spine dynamics.

Keywords: Calcium, astrocytes, interlaminar, iPSC, cortex, primate, dendritic spines

1. INTRODUCTION

Astrocytes, a subtype of glial cells in the central nervous system (CNS), are crucial for maintaining CNS homeostasis [1].They are intricately involved in neural circuits and influence various aspects of CNS function, including the regulation of neuronal development, synaptic transmission, ionic homeostasis, neurotransmitter recycling, metabolic regulation, and the maintenance of the blood-brain barrier [2-4]. Astrocyte excitability is manifested as elevations of cytosolic Ca^{2+}. Astrocyte Ca^{2+} elevations can occur spontaneously as intrinsic oscillations in the absence of neuronal activity, can be triggered by neurotransmitters released during synaptic activity and can occur in response to sensory stimulation [5]. Increasing evidence highlights the heterogeneity of astrocyte functions, which arise from diverse morphologies and transcriptomic profiles across different brain regions [6]. However, much of this knowledge comes from studies on rodent astrocytes, which differ from their human counterparts in several key aspects [7-9], leaving the structural and functional properties of human astrocytes largely unexplored.

In comparison to rodents, human astrocytes exhibit distinct genomic profiles, larger territories, more complex morphologies, faster intracellular Ca^{2+} signaling, and morphological features unique to primates [8-10]. Astrocyte subtypes are regionally distributed within the brain, including protoplasmic astrocytes in the gray matter, fibrous astrocytes in the white matter, and other types such as velate astrocytes, perivascular astrocytes, Müller cells, and Bergmann glia [1]. Additionally, higher-order primates and humans possess astrocyte subtypes like interlaminar and varicose projection astrocytes, which are not found in rodents [1, 8, 11-13]. In the human cortex, interlaminar astrocytes (ILAs) reside in layer I and extend long processes that traverse multiple cortical layers, terminating in layers III/IV [12, 14]. While rudimentary interlaminar astrocytes can also be found in the rodent cortex, their processes are shorter and do not extend beyond layer I [12]. The functional roles of primate-specific interlaminar astrocytes in the development, maintenance, and function of cortical neural circuits remain poorly understood.

We recently developed a chimeric mouse model with human-induced pluripotent stem cell (hiPSC)-derived astrocytes, in which interlaminar astrocytes (ILAs) are present in the mouse cerebral cortex [15]. This model offers the first opportunity to investigate the functional properties

of ILAs. In this study, we conducted Ca^{2+} imaging of ILA processes both in brain slices and *in vivo*, assessing their responses to canonical neurotransmitters. To assess a potential contribution of ILAs to neurodevelopmental disorders, we also engrafted astrocytes derived from hiPSCs of individuals with Fragile X syndrome (FXS), the most common inherited form of autism spectrum disorders. Given our previous findings that cultured astrocytes derived from FXS hiPSCs exhibit hyperexcitable Ca^{2+} signaling [16], we compared the Ca^{2+} signaling between FXS and control ILAs. Additionally, using multiphoton imaging of dendritic spines, we observed that dendrites near FXS ILAs have higher spine turnover rates compared to those near control ILAs suggesting the FXS ILAs contribute to altered synaptic plasticity in FXS.

2. METHODS

Mice

Mice were cared in accordance with NIH guidelines for laboratory animal welfare. All protocols were approved by the University of Nebraska Medical Center (UNMC) Institutional Animal Care and Use Committee. Rag1 immunodeficient mice (B6.129S7-*Rag1*^{tm1Mom}/J, Jackson Laboratory, IMSR Cat# JAX: 002216, RRID: IMSR_JAX: 002216) were bred at the UNMC facility with a 12-hr light/dark cycle with food and water available ad libitum.

Stem cell differentiation

The FX11-9u (RRID: CVCL_EJ77), FX11-7 (RRID: CVCL_EJ76) hiPSC lines, and WA01 (RRID: CVCL_9771), H1-FMR1-KO hESC lines were obtained from WiCell. The FX11-9u and FX11-7 hiPSC lines were derived from the same FXS patient. The FX11-9u line retained the FMRP expression due to the mosaicism of CGG repeats during reprogramming [17]. The H1-FMR1-KO (abbreviated as FMR1-KO) was engineered by CRISPR/Cas9 targeting exon 3 of the FMR1 gene in WA01 [18]. The SC176 control line was a gift from Dr. Gary Bassell [19]. The same protocol as previously described [15, 16] was used for RFP transduced cells. For the GCaMP6f and mScarlet transduced cells, the embryoid bodies were generated by treatment of hiPSCs with ReLeSR™ (STEMCELL Technologies) and passing the clumps though a 100 µm sterile strainer.

Viral transduction

NPCs were transfected with CMV-RFP lentivirus (Cellomics Technologies) or LV-CMV-GCaMP6f-T2A-mScarlet (SignaGen Laboratories) as previously described [15] with the modification that transduced NPCs were expanded prior to differentiation to astrocytes for all cells except those transduced with CMV-RFP.

Engraftment of human iPSC derived astrocytes

Engraftment was performed as previously described [15]. Briefly, $Rag1^{-/-}$ neonatal mice (both males and females) were transplanted on postnatal day 1 with hiPSC-derived astrocytes expressing GCaMP6f and mScarlet or RFP. The pups were cryoanesthetized for 4 min and transferred to a neonatal stage (Stoelting) that was cooled to 4°C during the stereotaxic injections. For cortical labeling, the pups were injected directly through the skin into two sites: AP -1.0 and -2.0, ML ± 1.0 mm, ventral 0.2-0.8mm, 10,000 cells/µl per site using a Hamilton syringe.

Brain slice preparation

At 6 months following hiPSCs-Astrocyte (hi-Astrocyte) engraftment, anesthetized mice (Avertin, 0.25 mg/g body weight) were transcardially perfused with carbogenated (95% O_2/5% CO_2) N-Methyl-D-glucamine (NMDG) artificial cerebrospinal fluid (aCSF) containing (in mM) 92 NMDG, 2.5 KCl, 1.25 NaH_2PO_4, 30 $NaHCO_3$, 20 HEPES, 25 glucose, 2 thiourea, 5 Na-ascorbate, 3 Na-pyruvate, 0.5 $CaCl_2$ and 10 $MgSO_4$. Following perfusion, mice were decapitated and their brains quickly removed and immersed in ice-cold carbogenated aCSF. Acute coronal slices containing the frontal cortex were cut to 300 µm using a vibratome. The slices were transferred into a pre-warmed chamber containing carbogenated NMDG aCSF and held for 10 minutes at 32–34 °C. After this initial recovery period, the slices were transferred into a new holding chamber containing room-temperature recording aCSF containing (in mM) 119 NaCl, 2.5 KCl, 1.25 NaH_2PO_4, 24 $NaHCO_3$, 12.5 glucose, 2 $CaCl_2$ and 2 $MgSO_4$ under constant carbogenation and held in this chamber for at least 1 hour before the imaging commenced. For imaging, slices were transferred to the submersion-type chamber and superfused at room temperature (22–24 °C) with recording aCSF saturated with 95% O_2/5% CO_2.

For the Ca^{2+} imaging data shown for 4 months following hi-Astrocyte engraftment, anesthetized mice were transcardially perfused with carbogenated aCSF. Acute coronal slices were cut in carbogenated aCSF containing (in mM) 126 NaCl, 3 KCl, 1.25 NaH_2PO_4, 4 $MgSO_4$, 2 $CaCl_2$, 26 $NaHCO_3$, and 10 dextrose. The slices were transferred into a holding chamber containing room-temperature recording aCSF containing (in mM) 126 NaCl, 3 KCl, 1.25 NaH_2PO_4, 1 $MgSO_4$, 2 $CaCl_2$, 26 $NaHCO_3$, and 10 dextrose.

Dye loading in slices

Following a recovery period, slices were loaded with Fluo-4 AM (5 µM) and 0.6 µL of Pluronic acid F-127 diluted in 1.5ml of aCSF (containing 1 mM Mg^{2+}) saturated with 95% O_2/5% CO_2 for 40 minutes at room temperature. Following three 10 minutes washes with aCSF, the slices for imaging were transferred to the submersion-type recording chamber and superfused at room temperature (22–24°C) with aCSF saturated with 95% O_2/5% CO_2 containing.

Viral injection and cranial window implantation

To perform *in vivo* multiphoton imaging of eGFP expressing mouse neurons in the vicinity of RFP-expressing human astrocytes, we performed viral injection into Layer 2/3 of the cortex and implanted a cranial window in 3.5 -month-old chimeric mice [20]. To visualize Ca^{2+} activity in vivo, a cranial window was implanted in 6-month-old chimeric mice expressing GCaMP6f and mScarlet. Mice were injected twice daily with 5 mg/kg enrofloxacin for 6 days and 5 mg/kg carprofen daily for 20 days. Mice were allowed three weeks to recover from the surgery prior to imaging.

Multiphoton imaging

Slice imaging and pharmacology

Time-lapse imaging was performed with a two-photon microscope (Moving Objective Microscope (MOM), Sutter) attached to a Ti : sapphire laser (Chameleon Vision II, Coherent) using a 25x water immersion objective (1.05 NA, Nikon) and equipped with a resonant scanner and a piezo stage (nPFocus400, nPoint). Excitation wavelength was tuned to 920 nm with 10-12 mW power as measured at the back aperture. Two-channel detection of emission wavelength

was achieved by using a 670 nm dichroic mirror and two external photomultiplier tubes (GaAsP) . A 535/50 bandpass filter was used to detect GCaMP6f emission wavelength, and a 610/75 bandpass filter was used to detect mScarlet or RFP. For imaging, we used ScanImage software (Vidrio) written in MATLAB (The MathWorks) [21]. Images of ILA were acquired at a resolution of (0.3 µm/pixel), a 20 µm volume at a step size of 1 µm and a frame rate of 1Hz. Time-lapse imaging was performed for a period of 5 minutes. For each slice, two minutes of spontaneous Ca^{2+} activity was recorded first, followed by agonist application for 2 minutes. Agonists were added to the perfusing ACSF at the following final concentrations: 100 µM ATP, 50 µM norepinephrine (NE) and 50 µM carbachol.

In vivo imaging

Dendritic spine imaging: On the imaging day, four-month-old chimeric mice were anaesthetized with a ketamine/dexdormitor mixture (100 mg/mL and 0.5 mg/mL, respectively, dosage 2.5mL/kg). Excitation power measured at the back aperture of the objective was typically around 20 mW and was adjusted to achieve near identical levels of fluorescence for each imaged region. Each optical section was collected at 512 x 512 pixels (0.186 µm/pixel). During an imaging session, 5 to 10 ROIs per animal were selected along with the apical dendritic tufts of eGFP expressing neurons within the vicinity of the RFP expressing human astrocytes in the cortex. Each ROI consisted of a stack of images (50-80 optical sections, separated axially by 1 µm). The coordinates of each ROI were recorded using the XYZ motor on the MOM for subsequent imaging days. After imaging, mice were revived from anesthesia with antisedan (atipamezole hydrochloride 5.0 mg/mL). Dendritic spines were imaged twice, at a four-day interval.

In vivo calcium imaging:

Mobile home cage (MHC, Neurotar) was used for imaging in awake mice where a head-fixed mouse can move around in an air-lifted MHC that features a flat floor and tangible walls and explore the environment under stress-free conditions. Prior to the imaging experiment, the mouse was habituated to the MHC by gradually increasing the duration of the habituation sessions every day and acclimating the mouse to the sounds of the laser scanning mirrors [20]. The habituation phase was started two weeks after the cranial window was implanted. Time-

lapse imaging was performed every 2s for a period of 5 minutes. Each optical section was collected at 512 × 512 pixels, 0.37 µm/pixel and a 20 µm volume was acquired at a step size of 1 µm.

Image Analysis

Process length analysis was performed as previously described [15]. Briefly, in each section multiple 5-pixel broad straight lines, 150–200 µm apart, were drawn from the pial surface to the deeper layer. For each line, the plot profile function was used to estimate the pixel intensity values along the line. The location of the last peak of RFP fluorescence was used as a measure of the extent to which processes traversed across the cortex and averaged per section. The values from control FX11-9u line were previously published [15].

Analysis of astrocytic Ca^{2+} events

The images acquired as a 20-micron volume were maximum intensity z projected in 5 micron volumes for further analysis. For proportion of active ILA processes upto 10 processes per field of view were scored as to whether they were responsive to an agonist. Event-based analysis of astrocyte Ca^{2+} image events was performed using Astrocyte Quantitative Analysis (AQuA) software [22] only on a subset of well isolated processes (1-3 per field of view). The AQuA-detected events were categorized based on area of the Ca^{2+} events with 3< 10 μm^2 (small) and >10 (large). Not all fibers displayed both small and large sized events. For analysis of astrocytic Ca^{2+} activity in the soma, a region of interest was outlined around the soma. The Ca^{2+} events were categorized into spontaneous and agonist-evoked events. The maximal amplitude (dF/F), area under the curve, duration (at half width), rise time (10-90) and decay time (90-10) of the events were analyzed. Clampfit v10.6 (pCLAMP, Molecular Devices) software was used to detect and measure the parameters for the soma.

Analysis of spine plasticity

The analysis of spine plasticity was performed on ImageJ software. For each image, dendrites with at least 25 µm-length, as well as located within 5 focal planes and 20 µm XY coordinates away from the RFP-expressing astrocytes were selected for further analysis. All spines on the

selected dendrites were counted and tracked over time to identify newly formed, eliminated and stabilized spines. Dendritic filopodia were distinguished as long dendritic protrusions with no head and were excluded from analysis (< 3% in both genotypes). Dendritic spines were analyzed by scrolling through individual z-planes within a stack. Spines were categorized as stable if they were present in the previous image as well as the one being analyzed, eliminated if they appeared in the previous image but not in the image being analyzed, newly formed as they appeared in the image being analyzed but not in the previous image. The percentage of spine formation and elimination was calculated using the number of newly formed or eliminated spines to the total number of spines analyzed in the image, respectively. Turnover rate (TOR) was calculated as the ratio of the sum of newly formed and eliminated spines to twice the total number of spines at baseline [23]. Analysis was performed on raw unprocessed images. For presentation purposes, images were despeckled and went through maximum intensity projection of 3–15 planes of focus.

Tissue preparation and confocal imaging

Mice were deeply anesthetized with TribromoEthanol (Avertin, 400mg/kg i.p.) and transcardially perfused with 4% paraformaldehyde in phosphate buffer (0.1 M) at 3 and 9 months post engraftment. The brain was dissected, post-fixed overnight, and 100 µm sagittal sections were cut on a vibratome in PBS. Confocal imaging of tissue sections was performed on a Nikon A1R upright microscope and images were acquired using a 20x (0.75 NA) objective. Images were collected at 512 × 512 pixels (with a pixel size of 1.24 µm) and a step size of 1 µm with 561 nm lasers.

Statistical analysis

Data were analyzed using GraphPad Prism. Outliers were removed using the ROUT approach. Normal distribution was tested using the Shapiro- Wilk test. Data are reported as mean ± S.E.M or median ± interquartile range. On scatter plots, medians are denoted by a thin line and means by a thick line. The following tests were conducted as appropriated: unpaired t-test, Mann-Whitney test and two-way ANOVA. P values was adjusted for multiple comparisons. For proportion of responding ILA processes a Chi-Square test was used.

3. RESULTS

Generation of hiPSCs-astrocyte chimeric mice

We differentiated human-induced pluripotent stem cells (hiPSCs) to neural progenitor cells (NPCs), and astrocytes subsequently [15, 24]. To visualize the hiPSC-astrocytes in the chimeric mouse brain and to measure astrocyte Ca^{2+} signaling, we generated RFP or mScarlet and GCaMP6f-expressing astrocytes. We previously demonstrated that prior to engraftment, RFP-expressing hiPSC-astrocytes showed robust expression of canonical astrocyte markers [15]. Two-site injection resulted in the widespread distribution of hiPSC-astrocytes in the frontal cortex. While at what we presume to be sites of injection both ILA and deeper protoplasmic astrocytes are observed, further away, cells are mainly confined to layer 1 and likely comprised both pial and subpial ILAs (Fig. 1A).

Calcium signaling properties of interlaminar astrocytes

The dynamic Ca^{2+} properties of the long ILA processes has not been previously examined. We therefore imaged slices at 6 months post engraftment in cells that expressed GCaMP6f and the structural marker mScarlet. At this age Ca^{2+} signals in both cell bodies in Layer 1 and the ILA processes that project from the pial surface could be examined (Fig. 1A). We performed volumetric 2-photon imaging of a 20-micron volume at 1 Hz to capture both spontaneous and drug induced changes (Fig.1B). We observed very little spontaneous activity with none of ILA soma exhibiting activity in absence of agonist. We next asked if hiPSC derived ILA cells are responsive to the canonical transmitters that have been examined extensively in mice; ATP (100 μM) to activate purinergic receptors, norepinephrine (NE, 50 μM) to activate noradrenergic receptors and carbachol (CA, 50 μM) to activate cholinergic receptors. We found that 56% and 44% of processes responded to ATP (n=141) and NE (n=100) respectively (Chi-Square, P=0.043). Interestingly, none of the ILAs responded to carbachol (data not shown). These data suggest that engrafted hi-Astrocytes that develop into ILAs express purinergic and adrenergic

receptors and the molecular machinery for Ca^{2+} signaling. However, the lack of response to carbachol suggest low or absent expression of cholinergic receptors on ILAs.

We next characterized the properties of the Ca^{2+} signals in soma and the processes. ILA soma, from engrafted control hi-Astrocytes, had robust Ca^{2+} responses to both ATP and NE that lasted for tens of seconds (Fig. 1 and 2A, B). We did not observe a difference in the peak amplitude of dF/F, area under the curve or the duration of the ATP- and NE-induced responses (Fig. 2A).
We next analyzed the Ca^{2+} events in the long ILA processes using AQUA. Since ILAs don't appear to have fine processes that are found on protoplasmic astrocytes, we only considered event sizes larger than 3 μm^2 and found that following ATP or NE application Ca^{2+} events spanned a range of 3-105 μm^2 however the distribution of ATP-induced Ca^{2+} was shifted towards larger events compared to NE-induced events (Fig. 2C, Kolmogorov-Smirnov test, P=0.025). The maximum event size is constrained by the length of the outlined processes that are observed within the slices. However, the larger event areas with ATP were not due to longer regions of interest, as in fact they were longer in the NE treated slices (ATP: 90.5±3.7 µm (n=28); NE: 106.4±3.5 µm (n=30), unpaired t-test P=0.003). We next characterized the Ca^{2+} signaling properties based on event sizes dividing them into small (3-10 μm^2) and large events (>10 μm^2). Despite the difference in the event areas, the dynamic properties of the ATP- and NE-induced Ca^{2+} events were not different in any of the parameters examined (Fig. 2D). These studies demonstrate that the long ILA processes exhibit Ca^{2+} signaling in response to canonical agonists.

To determine if the Ca^{2+} signaling observed in ILA processes occur in the intact brain, we performed 2-photon in vivo imaging of hi-Astrocyte engrafted mice through a cranial window in awake head-restrained conditions. Similarly to the observed Ca^{2+} activity in slices, we observed that long, thin processes in cortical Layer 1 exhibited robust Ca^{2+} responses in vivo (Fig. 1E). The activity is likely to be induced by the movement of the mouse.

ILA process length is not significantly altered in FXS

Impairments in astrocyte function is increasingly associated with neurodevelopmental disorder [25]. However, how ILAs that are specific to humans and non-human primates are altered in

neurodevelopmental disorders has not been examined before. We have utilized the human astrocyte mouse chimera model with astrocytes derived from FXS hiPSC or hiPSCs with deletion of FMR1 to determine if ILA development and function is altered. We have previously described the gradual development of ILA processes in the engrafted mice with few processes observed at 3 month and full palisade like processes observed at 9 months of age [15]. Here we first asked if process length was altered in FXS ILAs. Due to the large number of processes in the "palisade-like" distribution, we were unable to reliably track the processes of individual cells. Instead, we measured the distance of the "interlaminar palisade" from the pial surface in FX11-9u (CTR) and FX11-7 (FXS) hiPSC-astrocyte engrafted mice at three and nine months of age (Fig. 3). While the processes displayed a significant age factor ($F(2,40)=16.55$, $P<0.0001$) and FXS ILA processes tended to be longer, the genotype factor was not significant ($F(1,40)=3.129$, $P=0.08$) nor was there a significant interaction ($F(2, 40) = 0.7415$, $P=0.48$) (3 months: 145.00 ± 38.81 and 228.9 ± 29.90 µm and 9 months: 572.7 ± 81.49 and 673.4 ± 89.44 µm). Thus, we conclude that there was no gross alteration in the development of ILAs in FXS.

FXS ILAs have exaggerated calcium signaling

We next asked if FXS ILAs have altered Ca^{2+} signaling dynamics. At 4 months after engraftment, acute coronal slices were prepared from chimeric mice engrafted with FX11-9u and FX11-7 hiPSC-astrocytes. We focused on RFP-expressing cells in the cortical layer I near the pial surface. At this stage, interlaminar processes were not readily observed in slices. ATP-induced (100 µM) Ca^{2+} transients in the soma of RFP-expressing astrocytes detected by Fluo-4 AM were captured with multiphoton imaging (Fig. 4). Given the heterogeneity of engrafted astrocytes, with some not expressing RFP, the proportion of responding cells was not calculated. Unlike in slices from 6 month old engrafted mice where single response had single peaks (Fig. 2B), in slices with younger mice multi-peak Ca^{2+} transients in hiPSC-astrocytes were observed. There was no difference in frequency (the number of peaks per responding cell) nor difference in duration of responses (Fig. 4). However, consistent with previously published in vitro result [16], exaggerated Ca^{2+} signaling in the form of increased peak amplitude was observed in engrafted FXS hiPSC-astrocytes in slices (Fig. 4B, CTR: 77.46 ± 8.76 %dF/F, FXS: 118.8 ±6.5 %dF/F, $P = 0.0023$, N = 6-8 slices from 4-5 mice in each group).

We next examined Ca^{2+} signaling in 6-month-old chimeric mice that had developed ILA processes. For these experiments we engrafted mScarlet and GCaMP6 expressing hi-astrocytes derived from two FXS lines and the same three control lines and compared responses to ATP and NE. Unlike in younger mice, at 6 months of age we did not observe a difference between the peak amplitude of the soma responses to either ATP or NE between control and FXS cells (Fig. 5A and 6A). Instead, the soma of FXS ILAs had approximately 60% and 100% increase in the duration of the response to ATP and NE respectively ($P<0.001$ for both). Analysis of the ILA processes revealed no difference in the size of the area of ATP- and NE -induced Ca^{2+} events detected by AQUA between CTR and FXS (Fig. 5C and 6C). Analysis of small and large ILA processes determined that while most parameters were similar between CTR and FXS (Fig. 5D and 6D), a 62% increase in the duration of large ILA processes in response to ATP was observed in FXS ($P<0.05$). Overall, these data indicate hyperactive calcium signaling in FXS ILAs.

Increased dendritic spine turnover in mice engrafted with FXS ILAs

Cumulative evidence showed that astrocytes regulate spine formation and elimination to maintain dynamic and precise neuronal connections. Previous studies identified increased spine dynamics in the *Fmr1* KO mice [23, 26, 27]. Several studies described the contribution of astrocytes to the neuronal abnormalities in the mouse model of FXS [28-31]. Thus, we asked whether human astrocytes contribute to the altered spine plasticity in FXS by repeatedly imaging the same neuronal dendritic segments in vivo in the chimeric mice. Excitatory neurons in the chimeric mice were labeled with eGFP through viral injection [20]. Dendritic spines in proximity of RFP expressing hiPSC-astrocytes (distance < 20 μm) were imaged through the cranial window twice with 4-day interval (Fig. 7A). Dendritic spine density on dendrites in vicinity of FXS hiPSC-astrocytes showed a trend towards increased density (Fig. 7B, CTR: 2.41± 0.21, FXS: 3.24 ± 0.23, $P = 0.082$).

Though there was only a trend towards an increased percentage of newly formed dendritic spines in the FXS group compared with that in the CTR group (Fig. 7C, CTR: 27.90 ± 4.69 %,

FXS: 37.86 ± 4.11 %, P = 0.163, N = 16-28 regions from 4-5 mice in each group), the percentage of spine elimination on dendrites in FXS group was higher than that in CTR group (Fig. 7D, CTR: 20.08 ± 2.70 %, FXS: 30.26 ± 2.10 %, P = 0.003) as was the turnover rate (TOR) [23, 32](Fig. 7E, CTR: 0.23 ± 0.02, FXS: 0.33 ± 0.02, P = 0.037). These results demonstrate an increase in host dendritic spine plasticity attributed to engrafted FXS human astrocytes, indicating the role of astrocytes in the spine dynamics in FXS.

DISCUSSION

We used hiPSCs-astrocyte chimeric mice to characterize the Ca^{2+} signaling properties of ILAs and show Ca^{2+} increases in both the cell bodies and processes. We also for the first time rreport the capacity of ILA processes to respond to both purinergic and noradrenergic stimulation. Although we observed no gross alterations in the development of ILA processes in FXS, ILAs exhibited enhanced ATP and NE evoked Ca^{2+} signaling. Finally, using in vivo two- microscopy we show increased spine elimination and turnover rates in the host dendrites in the vicinity of FXS ILAs. We conclude that Ca^{2+} signaling is altered in FXS ILAs and that the increase in the host dendritic spine plasticity is attributed to the FXS ILAs indicating the role of astrocytes in the spine dynamics in FXS.

Studies using human brain tissue and human glial chimeric mice have shown differences in Ca^{2+} wave propagation between human and mouse astrocytes [8, 33]. The study by Oberheim and coworkers showed that the cell bodies and processes of human astrocytes responded to ATP. The Ca^{2+} imaging studies were performed on slices that were bulk loaded with the Ca^{2+} indicator dye fluo-4 AM to assess the evoked responses in human astrocytes. However, Fluo-4 only allows visualization and quantification of Ca^{2+} signals in soma and proximal processes [34] and is likely to conceal the Ca^{2+} events in the ILA processes. Our study utilized the genetically encoded Ca^{2+} indicator GCaMP6f that overcomes this limitation thereby revealing the Ca^{2+} signals in the ILA processes. Our study is the first to show Ca^{2+} signaling in the ILA processes in slices and in vivo. Rodent astrocytes respond to extracellular ATP and sensory input via elevations of intracellular calcium concentrations [35-37]. Astrocytic metabotropic (P2Y) and ionotropic (P2X) purinoreceptors are activated by ATP [1, 38]. The transcriptomic study from Zhang et al (2016)

showed that mRNA expression of P2RY1, P2RY12, and P2RY13 were present in human mature astrocytes with a higher expression of P2RY1. While P2Y1 receptors are linked to PLC/IP3/Ca^{2+} signaling cascade, P2Y12 and P2Y13 receptors are linked to Gi proteins and inhibit adenylyl cyclase activity [1]. Interestingly, P2Y12 receptor protein expression has been observed in ILA processes in multiple sclerosis patients [39]. Low mRNA expression of P2RX4 and P2RX7 in human mature astrocytes has also been observed [9]. It is likely that the ATP-evoked Ca^{2+} increases that we observe in the ILA soma and processes is mediated by activation of one or more of these purinoreceptor subtypes that participate in the mobilization of intracellular Ca^{2+} stores.

Astrocyte α1-adrenoreceptor are primary targets for norepinephrine that are coupled into Gq signaling pathways which trigger increases in Ca^{2+} in rodent astrocytes following startling stimuli or the activation of LC neurons using electrical stimulation [35, 37, 40, 41]. The α2 and β-adrenoreceptors are coupled to G_i and Gs signaling pathways respectively [42]. Human data indicate ADRA1A, ADRA1B, ADRB1 and ADRB2 mRNA expression in mature astrocytes with a higher expression of ADRB1 and ADRB2 [9]. The norepinephrine-evoked Ca^{2+} increases observed in the ILA soma and processes is likely to be mediated by activation of α1-adrenoreceptor.

Rodent astrocytes have been shown to elicit Ca^{2+} responses with carbachol application that activates G protein-coupled muscarinic receptors (Shelton and McCarthy, 2000). Human data indicate almost negligible levels of muscarinic cholinergic receptors and low mRNA expression for the nicotinic cholinergic receptor CHRNA4, CHRNA5 and CHRNA7. We observed no responses in either the ILA soma or processes with carbachol application indicating the absence of functional muscarinic receptors. Put together, our data show that the ILAs in the chimeric mouse have functional purinergic and adrenergic receptors. Ca^{2+} elevation and propagation along the ILA processes is of potential importance as this may facilitate long-distance coordination of intracortical communication.

Long dendritic spines with immature morphologies and higher density have been observed in the postmortem brain tissue of FXS patients [43, 44]. Dendritic spine abnormalities reported in the Fmr1 KO mouse model parallel abnormalities reported in FXS patients [45, 46]. Fmr1 KO mice have increased rates of dendritic spine formation, elimination and turnover [23, 26, 27, 47].

Astrocytes have emerged as important regulators of synapse development and have been shown to promote both synapse formation and maturation [2]. Astrocytes can influence both synaptogenesis and synapse maturation through secretion of astrocytic soluble factors and the expression of these proteins has been found to be altered in Fmr1 KO mice, possibly contributing to abnormal neuronal development and altered connectivity observed in FXS [48-51]. Astrocyte-specific loss of FMRP expression has been reported to result in increased dendritic spine formation. These rodent studies have contributed to increasing evidence that astrocytes play essential roles in modulating the function of neurons and neural circuits.

Human astrocytes are more complex than their mouse counterparts, and abnormalities observed in *Fmr1* KO astrocytes need to be replicated in human models. Altered structural properties of ILA has been found in other neurodevelopmental disorders. A postmortem study in children with Down Syndrome showed a reduction in the number of ILA processes [52]. Our study in the chimeric mice did not observe alterations in ILA process length in FXS. Interestingly, dendritic spine density on the dendrites in the vicinity of the engrafted FXS human astrocytes was found to be higher. Increased dendritic spine elimination and turnover rate were also observed in the FXS group showing that spine dynamics in the host dendrites is altered due to the FXS human astrocytes. Our study is the first to demonstrate altered dendritic spine plasticity using the chimeric mouse model and further highlights the role of astrocytes in the spine dynamics in FXS.

References

1. Verkhratsky, A. and M. Nedergaard, *Physiology of Astroglia.* Physiol Rev, 2018. **98**(1): p. 239-389.
2. Farizatto, K.L.G. and K.T. Baldwin, *Astrocyte-synapse interactions during brain development.* Curr Opin Neurobiol, 2023. **80**: p. 102704.

3. Lawal, O., F.P. Ulloa Severino, and C. Eroglu, *The role of astrocyte structural plasticity in regulating neural circuit function and behavior.* Glia, 2022. **70**(8): p. 1467-1483.
4. Lia, A., et al., *Two decades of astrocytes in neurovascular coupling.* Front Netw Physiol, 2023. **3**: p. 1162757.
5. Veiga, A., et al., *Calcium-Dependent Signaling in Astrocytes: Downstream Mechanisms and Implications for Cognition.* J Neurochem, 2025. **169**(2): p. e70019.
6. Khakh, B.S. and B. Deneen, *The Emerging Nature of Astrocyte Diversity.* Annu Rev Neurosci, 2019. **42**: p. 187-207.
7. Oberheim, N.A., S.A. Goldman, and M. Nedergaard, *Heterogeneity of astrocytic form and function.* Methods Mol Biol, 2012. **814**: p. 23-45.
8. Oberheim, N.A., et al., *Uniquely hominid features of adult human astrocytes.* J Neurosci, 2009. **29**(10): p. 3276-87.
9. Zhang, Y., et al., *Purification and Characterization of Progenitor and Mature Human Astrocytes Reveals Transcriptional and Functional Differences with Mouse.* Neuron, 2016. **89**(1): p. 37-53.
10. Oberheim, N.A., et al., *Astrocytic complexity distinguishes the human brain.* Trends Neurosci, 2006. **29**(10): p. 547-53.
11. Colombo, J.A., et al., *Immunocytochemical and electron microscope observations on astroglial interlaminar processes in the primate neocortex.* J Neurosci Res, 1997. **48**(4): p. 352-7.
12. Falcone, C., et al., *Cortical interlaminar astrocytes across the therian mammal radiation.* J Comp Neurol, 2019. **527**(10): p. 1654-1674.
13. Ciani, C. and C. Falcone, *Interlaminar and varicose-projection astrocytes: toward a new understanding of the primate brain.* Front Cell Neurosci, 2024. **18**: p. 1477753.
14. Colombo, J.A. and H.D. Reisin, *Interlaminar astroglia of the cerebral cortex: a marker of the primate brain.* Brain Res, 2004. **1006**(1): p. 126-31.
15. Padmashri, R., et al., *Modeling human-specific interlaminar astrocytes in the mouse cerebral cortex.* J Comp Neurol, 2021. **529**(4): p. 802-810.
16. Ren, B., et al., *Dysregulated cholesterol metabolism, aberrant excitability and altered cell cycle of astrocytes in fragile X syndrome.* Glia, 2023. **71**(5): p. 1176-1196.

17. Doers, M.E., et al., *iPSC-derived forebrain neurons from FXS individuals show defects in initial neurite outgrowth.* Stem Cells Dev, 2014. **23**(15): p. 1777-87.
18. Utami, K.H., et al., *Integrative Analysis Identifies Key Molecular Signatures Underlying Neurodevelopmental Deficits in Fragile X Syndrome.* Biol Psychiatry, 2020. **88**(6): p. 500-511.
19. Raj, N., et al., *Cell-type-specific profiling of human cellular models of fragile X syndrome reveal PI3K-dependent defects in translation and neurogenesis.* Cell Rep, 2021. **35**(2): p. 108991.
20. Padmashri, R., K. Tyner, and A. Dunaevsky, *Implantation of a Cranial Window for Repeated In Vivo Imaging in Awake Mice.* J Vis Exp, 2021(172).
21. Pologruto, T.A., B.L. Sabatini, and K. Svoboda, *ScanImage: flexible software for operating laser scanning microscopes.* Biomed Eng Online, 2003. **2**: p. 13.
22. Wang, Y., et al., *Accurate quantification of astrocyte and neurotransmitter fluorescence dynamics for single-cell and population-level physiology.* Nat Neurosci, 2019. **22**(11): p. 1936-1944.
23. Padmashri, R., et al., *Altered structural and functional synaptic plasticity with motor skill learning in a mouse model of fragile X syndrome.* J. Neurosci., 2013. **33**: p. 19715-19723.
24. Chen, C., et al., *Role of astroglia in Down's syndrome revealed by patient-derived human-induced pluripotent stem cells.* Nat Commun, 2014. **5**: p. 4430.
25. Sejourne, G. and C. Eroglu, *Astrocyte-neuron crosstalk in neurodevelopmental disorders.* Curr Opin Neurobiol, 2024. **89**: p. 102925.
26. Pan, F., et al., *Dendritic spine instability and insensitivity to modulation by sensory experience in a mouse model of fragile X syndrome.* Proc Natl Acad Sci U S A, 2010. **107**(41): p. 17768-73.
27. Suresh, A. and A. Dunaevsky, *Relationship Between Synaptic AMPAR and Spine Dynamics: Impairments in the FXS Mouse.* Cereb Cortex, 2017: p. 1-13.
28. Jacobs, S. and L.C. Doering, *Astrocytes prevent abnormal neuronal development in the fragile x mouse.* J Neurosci, 2010. **30**(12): p. 4508-14.
29. Yang, Q., et al., *Excessive astrocyte-derived neurotrophin-3 contributes to the abnormal neuronal dendritic development in a mouse model of fragile X syndrome.* PLoS Genet, 2012.

8(12): p. e1003172.

30. Hodges, J.L., et al., *Astrocytic Contributions to Synaptic and Learning Abnormalities in a Mouse Model of Fragile X Syndrome.* Biol Psychiatry, 2016. **s0006-3223 (16)**: p. 32779-2.
31. Higashimori, H., et al., *Selective Deletion of Astroglial FMRP Dysregulates Glutamate Transporter GLT1 and Contributes to Fragile X Syndrome Phenotypes In Vivo.* J Neurosci, 2016. **36**(27): p. 7079-94.
32. Holtmaat, A.J., et al., *Transient and persistent dendritic spines in the neocortex in vivo.* Neuron, 2005. **45**(2): p. 279-91.
33. Han, X., et al., *Forebrain engraftment by human glial progenitor cells enhances synaptic plasticity and learning in adult mice.* Cell Stem Cell, 2013. **12**(3): p. 342-53.
34. Shigetomi, E., et al., *Imaging calcium microdomains within entire astrocyte territories and endfeet with GCaMPs expressed using adeno-associated viruses.* J Gen Physiol, 2013. **141**(5): p. 633-47.
35. Ding, F., et al., *alpha1-Adrenergic receptors mediate coordinated Ca2+ signaling of cortical astrocytes in awake, behaving mice.* Cell Calcium, 2013. **54**(6): p. 387-94.
36. Nimmerjahn, A., E.A. Mukamel, and M.J. Schnitzer, *Motor behavior activates Bergmann glial networks.* Neuron, 2009. **62**(3): p. 400-12.
37. Paukert, M., et al., *Norepinephrine controls astroglial responsiveness to local circuit activity.* Neuron, 2014. **82**(6): p. 1263-70.
38. Fields, R.D. and G. Burnstock, *Purinergic signalling in neuron-glia interactions.* Nat Rev Neurosci, 2006. **7**(6): p. 423-36.
39. Amadio, S., et al., *P2Y12 receptor protein in cortical gray matter lesions in multiple sclerosis.* Cereb Cortex, 2010. **20**(6): p. 1263-73.
40. Bekar, L.K., W. He, and M. Nedergaard, *Locus coeruleus alpha-adrenergic-mediated activation of cortical astrocytes in vivo.* Cereb Cortex, 2008. **18**(12): p. 2789-95.
41. Srinivasan, R., et al., *Ca(2+) signaling in astrocytes from Ip3r2(-/-) mice in brain slices and during startle responses in vivo.* Nat Neurosci, 2015. **18**(5): p. 708-17.
42. Ramos, B.P. and A.F. Arnsten, *Adrenergic pharmacology and cognition: focus on the prefrontal cortex.* Pharmacol Ther, 2007. **113**(3): p. 523-36.
43. Hinton, V.J., et al., *Analysis of neocortex in three males with the fragile X syndrome.* Am. J.

Med. Genet., 1991. **41**: p. 289-294.

44. Irwin, S.A., et al., *Abnormal dendritic spine characteristics in the temporal and visual cortices of patients with fragile-X syndrome: a quantitative examination.* Am J Med Genet, 2001. **98**(2): p. 161-7.
45. Comery, T.A., et al., *Abnormal dendritic spines in fragile X knockout mice: maturation and pruning deficits.* Proc. Natl. Acad. Sci. U S A, 1997. **94**: p. 5401-4.
46. McKinney, B.C., et al., *Dendritic spine abnormalities in the occipital cortex of C57BL/6 Fmr1 knockout mice.* Am J Med Genet B Neuropsychiatr Genet, 2005. **136**(1): p. 98-102.
47. Cruz-Martin, A., M. Crespo, and C. Portera-Cailliau, *Delayed stabilization of dendritic spines in fragile X mice.* J Neurosci, 2010. **30**(23): p. 7793-803.
48. Cheng, C., S.K. Lau, and L.C. Doering, *Astrocyte-secreted thrombospondin-1 modulates synapse and spine defects in the fragile X mouse model.* Mol Brain, 2016. **9**(1): p. 74.
49. Wallingford, J., et al., *Altered Developmental Expression of the Astrocyte-Secreted Factors Hevin and SPARC in the Fragile X Mouse Model.* Front Mol Neurosci, 2017. **10**: p. 268.
50. Krasovska, V. and L.C. Doering, *Regulation of IL-6 Secretion by Astrocytes via TLR4 in the Fragile X Mouse Model.* Front Mol Neurosci, 2018. **11**: p. 272.
51. Reynolds, K.E., C.R. Wong, and A.L. Scott, *Astrocyte-mediated purinergic signaling is upregulated in a mouse model of Fragile X syndrome.* Glia, 2021. **69**(7): p. 1816-1832.
52. Colombo, J.A., et al., *Development of interlaminar astroglial processes in the cerebral cortex of control and Down's syndrome human cases.* Exp Neurol, 2005. **193**(1): p. 207-17.

Figure Legends

Figure 1: Imaging Ca^{2+} activity in the interlaminar astrocytes

Time-lapse imaging of ILA in a cortical slice from a 6-month-old chimeric mouse. **A.** ILAs expressing the structural marker mScarlet is shown. **B.** Ca^{2+} activity in ILA astrocytes expressing GCaMP6f. Individual representative frames are shown for ATP-evoked Ca^{2+} responses. **C.** AQuA-detected events in corresponding time frames shown in B. Propagation of the Ca^{2+} signal along the ILA process can be observed. **D.** In vivo imaging of ILA in an awake head restrained mouse. Shown here are mScarlet expressing ILA astrocytes. **E.** Time-lapse imaging of Ca^{2+} signals in ILA processes. **F.** AQuA-detected events in two corresponding time frames showing detected Ca^{2+} events. Scale bars: 25 µm.

Figure 2: Ca^{2+} activity in interlaminar astrocytes

A. ATP and NE-evoked Ca^{2+} activity in ILA soma in cortical slices. Data is shown for Ca^{2+} event amplitude, area under the curve and duration. N = 36 for ATP and N = 27. **B.** Example traces are shown for ATP- and NE-evoked Ca^{2+} signals. **C.** Frequency distribution for size of the Ca^{2+} events in ILA processes with ATP and NE application. Kolmogorov-Smirnov test, P=0.025. **D.** ATP and NE-evoked Ca^{2+} activity in ILA processes in cortical slices. Data is shown for Ca^{2+} event amplitude, area under the curve, duration, rise time to peak and decay time for small events (top panel) and large events (bottom panel). No significant differences were observed in Ca^{2+} signaling properties between ATP- and NE-evoked responses in the ILA processes. N = 20 fibers for ATP and N = 25 fibers for NE experiments, Multiple Mann-Whitney tests. Mean ± sem and median ± interquartile range are shown.

Figure 3: Interlaminar astrocyte process length is not altered in FXS

A. Control and FXS human astrocytes expressing RFP in the cortex of 3 and 9-month-old chimeric mice. Scale bar, 100 µm. **B.** Quantification of the distance traversed by CTR and FXS ILA processes in the 3 and 9-month-old chimeric mice. N = 5–9 sections from 2 to 3 chimeric mice per group. Two-way ANOVA. Age factor ($F(2,40)=16.55$, $P<0.0001$)

Figure 4: Enhanced ATP-evoked Ca^{2+} signaling in FXS astrocytes

A. Time-lapse imaging of CTR and FXS astrocytes in a cortical slice from a 4-month-old chimeric mouse. Images of RFP-expressing astrocytes (red) and time-lapse images of the fluo-4 channel (green) showing ATP-evoked Ca^{2+} responses (top panel: CTR, bottom panel: FXS). Traces for the Ca^{2+} responses are shown for the regions of interest (ROI 1-5) indicated in the RFP images. **B.** Peak amplitude of ATP-evoked Ca^{2+} responses is higher in FXS astrocytes. Mann-Whitney test. P = 0.0023. **C.** Frequency of ATP-evoked Ca^{2+} responses. Mann-Whitney test. P = 0.2699. **D.** Duration of ATP-evoked Ca^{2+} responses. Mann-Whitney test. P = 0.1807. N = 6-8 slices from 4-5 mice in each group.

Figure 5: Enhanced ATP-evoked Ca^{2+} signaling in FXS interlaminar astrocytes

A. ATP-evoked Ca^{2+} activity in soma of CTR and FXS ILAs in cortical slices. Data is shown for Ca^{2+} event amplitude, area under the curve and duration. FXS astrocyte soma exhibited increased Ca^{2+} event duration. N = 36 soma for CTR and N = 33 soma for FXS, multiple Mann-Whitney tests, P=0.0002 **B.** Example traces are shown for ATP-evoked Ca^{2+} signals in CTR and FXS ILA soma. **C.** Frequency distribution for size of the Ca^{2+} events in processes in CTR and FXS astrocytes. Kolmogorov-Smirnov test, P>0.05. **D.** ATP-evoked Ca^{2+} activity in ILA processes of CTR and FXS astrocytes in cortical slices. Data is shown for Ca^{2+} event amplitude, area under the curve, duration, rise time to peak and decay time for small events (top panel) and large events (bottom panel). A significant increase in the Ca^{2+} event duration for large events was observed in the FXS ILA processes. N = 20 processes for CTR and N = 26 processes for FXS, multiple Mann-Whitney tests P=0.029. Mean ± sem and median ± interquartile range are shown.

Figure 6: Enhanced NE-evoked Ca^{2+} signaling in FXS interlaminar astrocytes

A. NE-evoked Ca^{2+} activity in soma of CTR and FXS ILAs in cortical slices. Data is shown for Ca^{2+} event amplitude, area under the curve and duration. FXS astrocytes exhibited increased Ca^{2+} event duration and area under the curve. N = 27 for CTR and N = 12 for FXS, multiple Mann-Whitney tests, P=0.008 and P=0.006. **B.** Traces are shown for NE-evoked Ca^{2+} signals in CTR and FXS ILA soma. **C.** Frequency distribution for size of the Ca^{2+} events in processes in

CTR and FXS ILAs. Kolmogorov-Smirnov test, P>0.05. **D.** NE-evoked Ca^{2+} activity in ILA processes of CTR and FXS astrocytes in cortical slices. Data is shown for Ca^{2+} event amplitude, area under the curve, duration, rise time to peak and decay time for small events (top panel) and large events (bottom panel). No significant changes were observed in the FXS astrocyte processes. N = 18-25 processes for CTR and N = 6-10 processes for FXS, multiple Mann-Whitney tests.

Figure 7: Altered dendritic spine dynamics in chimeric mice with FXS ILAs

A. In vivo imaging of eGFP expressing mouse dendrites in the vicinity of CTR (top) and FXS (bottom) ILAs (distance < 20 μm on the x and y axis) in the cortex of 4-month-old chimeric mice. Repeated in vivo imaging was performed at two timepoints over a 4-day interval. Blue and yellow arrows point to eliminated and newly formed spines respectively. **B.** No differences were found in the dendritic spine density. Unpaired t-test, P = 0.08. **C.** No differences were found in dendritic spine formation. Unpaired t-test. P = 0.16. **D.** Increased spine elimination was observed in the dendrites in the vicinity of FXS ILAs. Unpaired t-test, P = 0.003. **E.** The turnover rates (TOR) were elevated in the dendrites in the vicinity of FXS ILAs. Unpaired t-test, P = 0.037, N = 16-28 regions from 4-5 mice in each group.

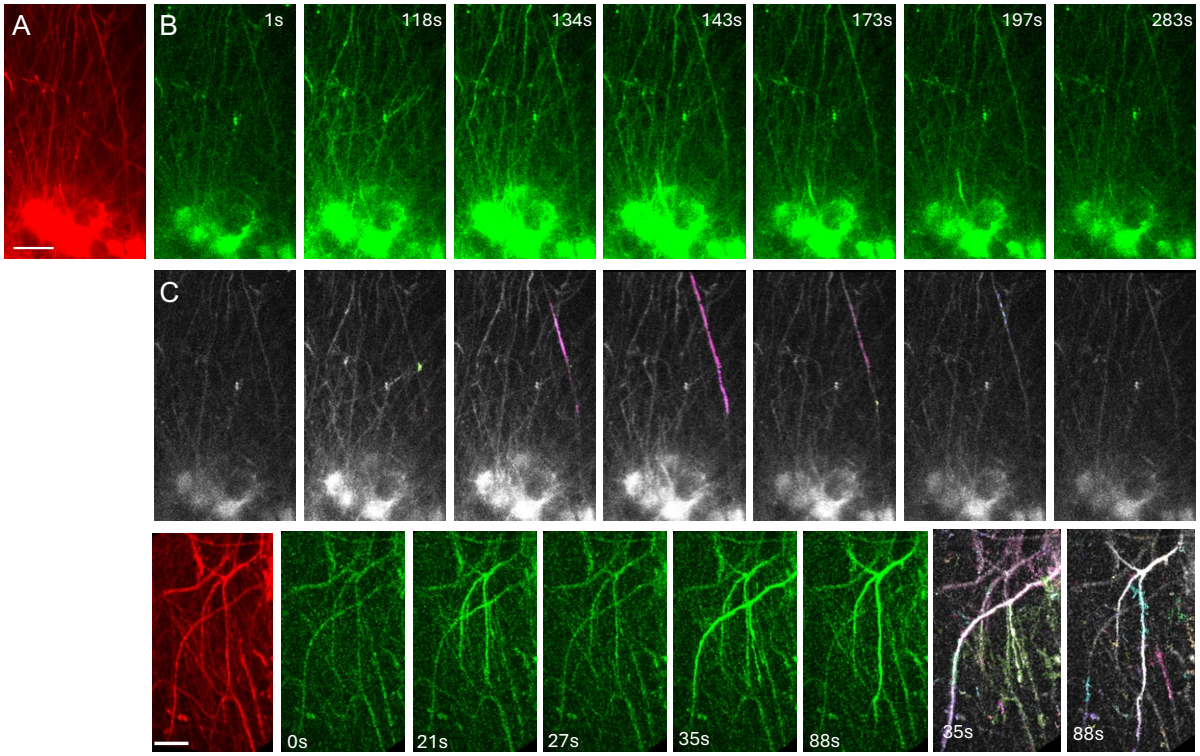

Figure 1: Imaging Ca^{2+} activity in the interlaminar astrocytes Time-lapse imaging of ILA in a cortical slice from a 6-month-old chimeric mouse. **A.** ILAs expressing the structural marker mScarlet is shown. **B.** Ca^{2+} activity in ILA astrocytes expressing GCaMP6f. Individual representative frames are shown for ATP-evoked Ca^{2+} responses. **C.** AQuA-detected events in corresponding time frames shown in B. Propagation of the Ca^{2+} signal along the ILA process can be observed. **D.** In vivo imaging of ILA in an awake head restrained mouse. Shown here are mScarlet expressing ILA astrocytes. **E.** Time-lapse imaging of Ca^{2+} signals in ILA processes. **F.** AQuA-detected events in two corresponding time frames showing detected Ca^{2+} events. Scale bars: 25 μm.

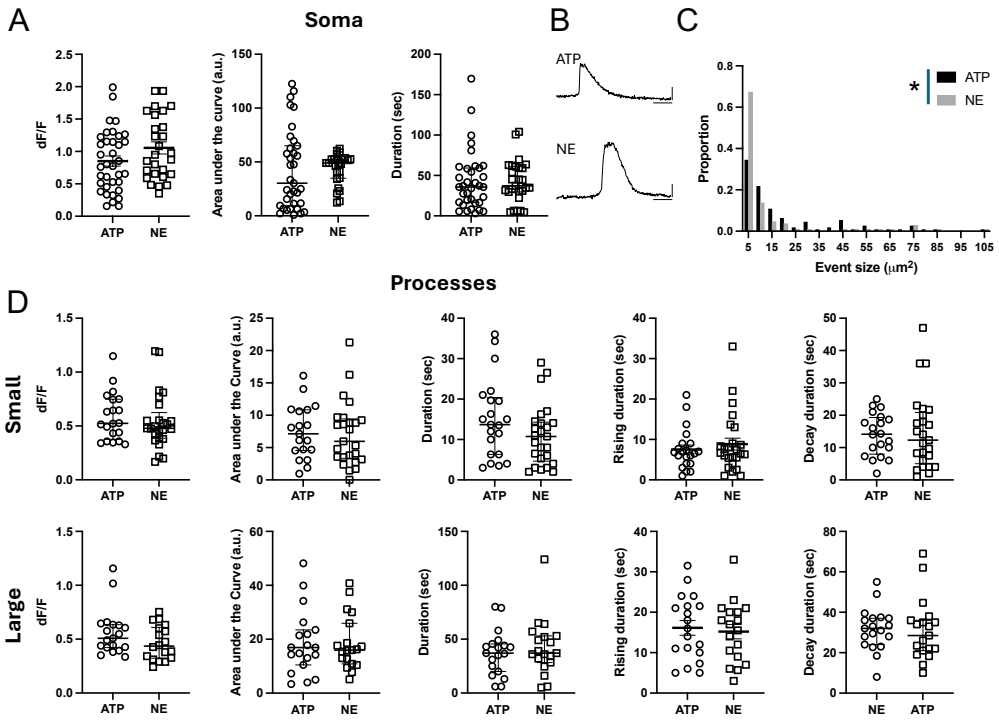

Figure 2: Ca^{2+} activity in interlaminar astrocytes A. ATP and NE-evoked Ca^{2+} activity in ILA soma in cortical slices. Data is shown for Ca^{2+} event amplitude, area under the curve and duration. N = 36 for ATP and N = 27. **B.** Example traces are shown for ATP- and NE-evoked Ca^{2+} signals. **C.** Frequency distribution for size of the Ca^{2+} events in ILA processes with ATP and NE application. Kolmogorov-Smirnov test, P=0.025. **D.** ATP and NE-evoked Ca^{2+} activity in ILA processes in cortical slices. Data is shown for Ca^{2+} event amplitude, area under the curve, duration, rise time to peak and decay time for small events (top panel) and large events (bottom panel). No significant differences were observed in Ca^{2+} signaling properties between ATP- and NE-evoked responses in the ILA processes. N = 20 fibers for ATP and N = 25 fibers for NE experiments, Multiple Mann-Whitney tests. Mean ± sem and median ± interquartile range are shown.

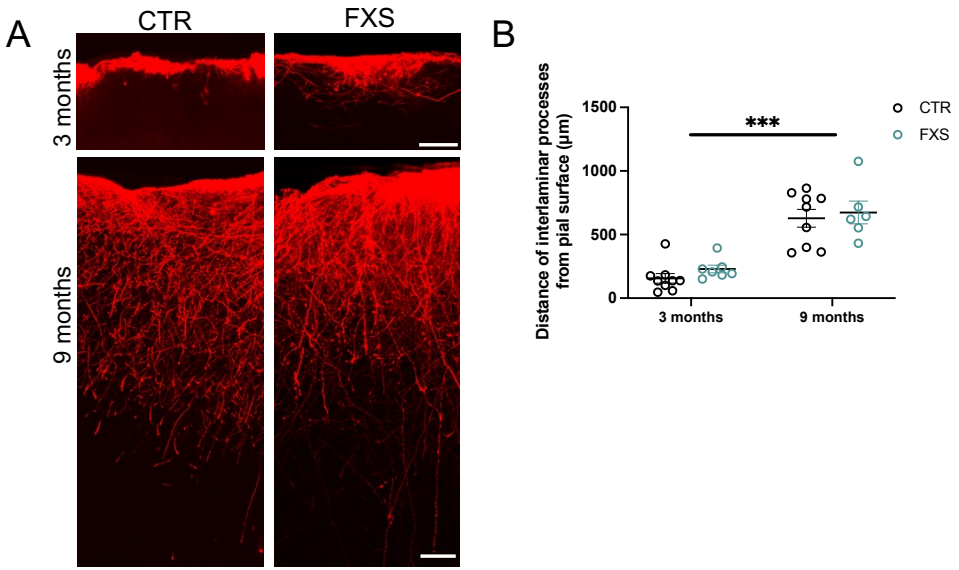

Figure 3: Interlaminar astrocyte process length is not altered in FXS A. Control and FXS human astrocytes expressing RFP in the cortex of 3 and 9-month-old chimeric mice. Scale bar, 100 µm. **B.** Quantification of the distance traversed by CTR and FXS ILA processes in the 3 and 9-month-old chimeric mice. N = 5–9 sections from 2 to 3 chimeric mice per group. Two-way ANOVA. Age factor ($F(2,40)=16.55$, $P<0.0001$)

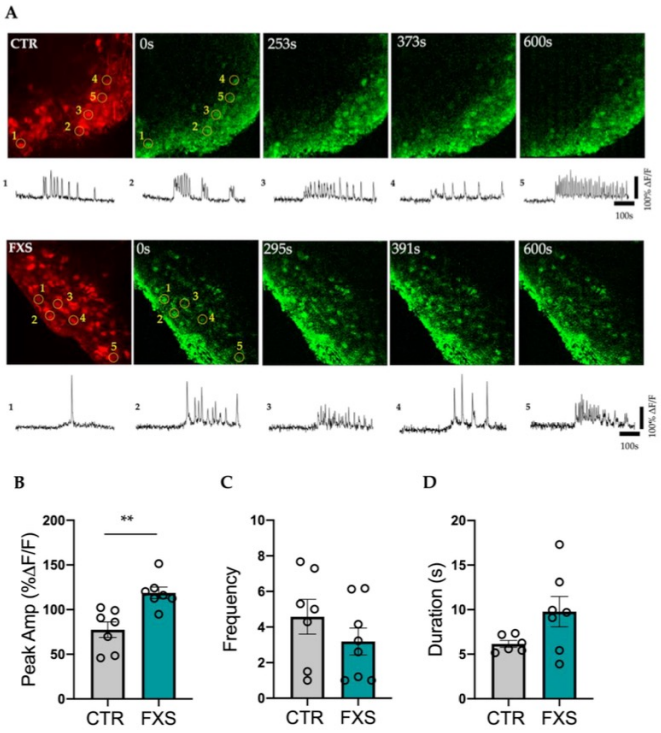

Figure 4: Enhanced ATP-evoked Ca^{2+} signaling in FXS astrocytes A. Time-lapse imaging of CTR and FXS astrocytes in a cortical slice from a 4-month-old chimeric mouse. Images of RFP-expressing astrocytes (red) and time-lapse images of the fluo-4 channel (green) showing ATP-evoked Ca^{2+} responses (top panel: CTR, bottom panel: FXS). Traces for the Ca^{2+} responses are shown for the regions of interest (ROI 1-5) indicated in the RFP images. **B.** Peak amplitude of ATP-evoked Ca^{2+} responses is higher in FXS astrocytes. Mann-Whitney test. P = 0.0023. **C.** Frequency of ATP-evoked Ca^{2+} responses. Mann-Whitney test. P = 0.2699. **D.** Duration of ATP-evoked Ca^{2+} responses. Mann-Whitney test. P = 0.1807. N = 6-8 slices from 4-5 mice in each group.

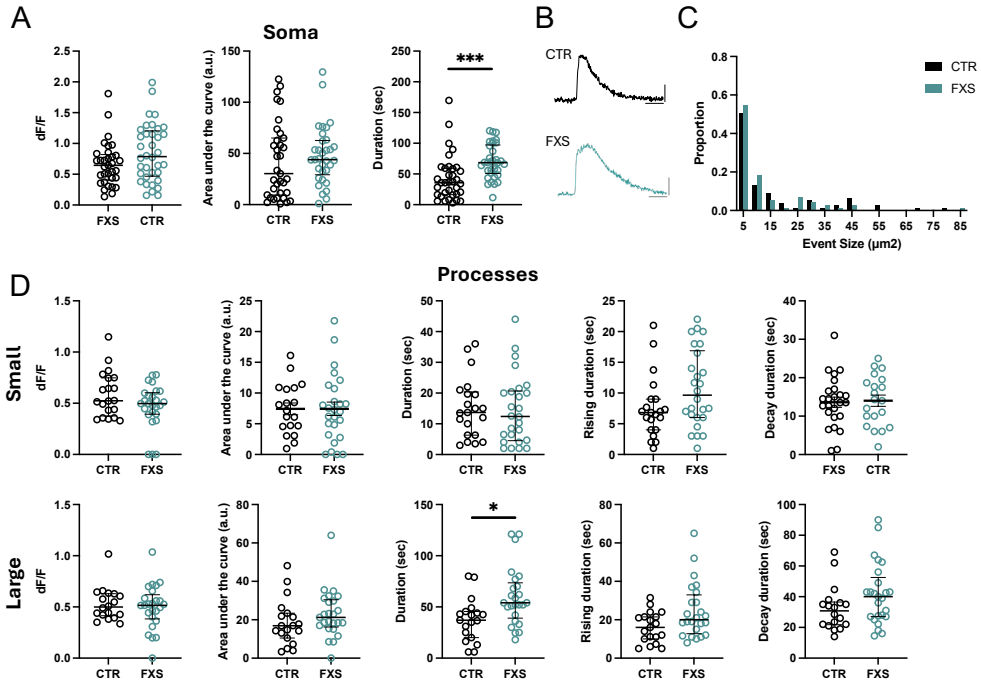

Figure 5: Enhanced ATP-evoked Ca^{2+} signaling in FXS interlaminar astrocytes A. ATP-evoked Ca^{2+} activity in soma of CTR and FXS ILAs in cortical slices. Data is shown for Ca^{2+} event amplitude, area under the curve and duration. FXS astrocyte soma exhibited increased Ca^{2+} event duration. N = 36 soma for CTR and N = 33 soma for FXS, multiple Mann-Whitney tests, P=0.0002 **B.** Example traces are shown for ATP-evoked Ca^{2+} signals in CTR and FXS ILA soma. **C.** Frequency distribution for size of the Ca^{2+} events in processes in CTR and FXS astrocytes. Kolmogorov-Smirnov test, P>0.05. **D.** ATP-evoked Ca^{2+} activity in ILA processes of CTR and FXS astrocytes in cortical slices. Data is shown for Ca^{2+} event amplitude, area under the curve, duration, rise time to peak and decay time for small events (top panel) and large events (bottom panel). A significant increase in the Ca^{2+} event duration for large events was observed in the FXS ILA processes. N = 20 processes for CTR and N = 26 processes for FXS, multiple Mann-Whitney tests P=0.029. Mean ± sem and median ± interquartile range are shown.

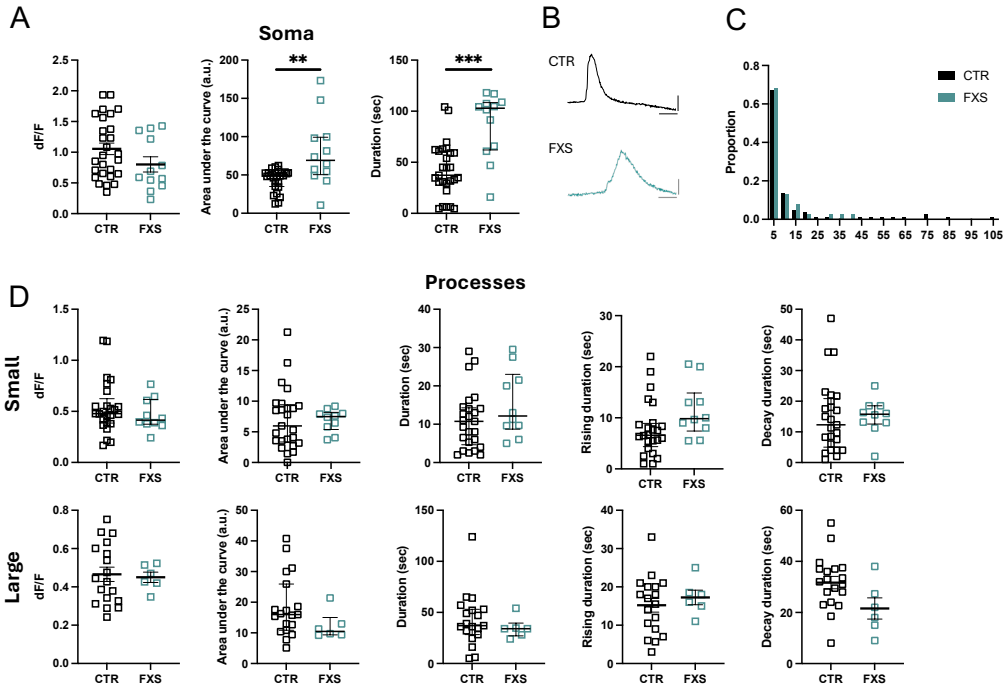

Figure 6: Enhanced NE-evoked Ca^{2+} signaling in FXS interlaminar astrocytes A. NE-evoked Ca^{2+} activity in soma of CTR and FXS ILAs in cortical slices. Data is shown for Ca^{2+} event amplitude, area under the curve and duration. FXS astrocytes exhibited increased Ca^{2+} event duration and area under the curve. N = 27 for CTR and N = 12 for FXS, multiple Mann-Whitney tests, P=0.008 and P=0.006. **B.** Traces are shown for NE-evoked Ca^{2+} signals in CTR and FXS ILA soma. **C.** Frequency distribution for size of the Ca^{2+} events in processes in CTR and FXS ILAs. Kolmogorov-Smirnov test, P>0.05. **D.** NE-evoked Ca^{2+} activity in ILA processes of CTR and FXS astrocytes in cortical slices. Data is shown for Ca^{2+} event amplitude, area under the curve, duration, rise time to peak and decay time for small events (top panel) and large events (bottom panel). No significant changes were observed in the FXS astrocyte processes. N = 18-25 processes for CTR and N = 6-10 processes for FXS, multiple Mann-Whitney tests.

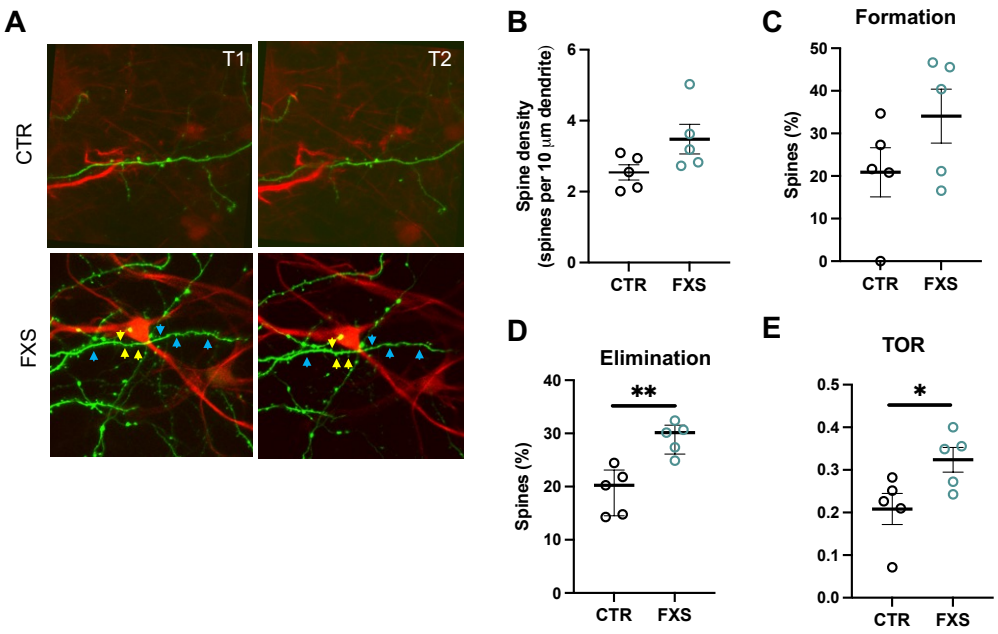

Figure 7: Altered dendritic spine dynamics in chimeric mice with FXS ILAs A. In vivo imaging of eGFP expressing mouse dendrites in the vicinity of CTR (top) and FXS (bottom) ILAs (distance < 20 μm on the x and y axis) in the cortex of 4-month-old chimeric mice. Repeated in vivo imaging was performed at two timepoints over a 4-day interval. Blue and yellow arrows point to eliminated and newly formed spines respectively. **B.** No differences were found in the dendritic spine density. Unpaired t-test, P = 0.08. **C.** No differences were found in dendritic spine formation. Unpaired t-test. P = 0.16. **D.** Increased spine elimination was observed in the dendrites in the vicinity of FXS ILAs. Unpaired t-test, P = 0.003. **E.** The turnover rates (TOR) were elevated in the dendrites in the vicinity of FXS ILAs. Unpaired t-test, P = 0.037, N = 16-28 regions from 4-5 mice in each group.